American Mineralogist, Volume 97, pages 430–439, 2012

Crystal chemistry of trioctahedral micas-2M_1 from Bunyaruguru kamafugite (southwest Uganda)

Fernando Scordari,* Emanuela Schingaro, Maria Lacalamita, and Ernesto Mesto

Dipartimento di Scienze della Terra e Geoambientali, Università degli Studi di Bari, via E. Orabona 4, I-70125 Bari, Italy

Abstract

The crystal chemistry of 2M_1 micas from Bunyaruguru kamafugite (southwest Uganda) was studied by electron probe microanalysis, single-crystal X-ray diffraction, Mössbauer and Fourier transform infrared spectroscopy. Chemical analyses showed that the studied crystals are Ti-rich, F-poor phlogopites with an annitic component, $Fe_{tot}/(Fe_{tot} + Mg)$, ranging from 0.15 to 0.22. Unit-cell parameters from single-crystal X-ray data are in the range: $5.3252(1) \le a \le 5.3307(1)$, $9.2231(3) \le b \le 9.2315(3)$, $20.1550(6) \le c \le 20.1964(8)$ Å, and $94.994(2) \le \beta \le 95.131(2)°$.

Anisotropic structure refinements, in the space group *C*2/*c*, converged to $2.77 \le R_1 \le 3.52\%$ and $2.91 \le wR_2 \le 4.02\%$. Mössbauer spectroscopy showed that the studied sample has: $^{VI}Fe^{2+} = 60(1)\%$, $^{VI}Fe^{3+} = 24(1)\%$, and $^{IV}Fe^{3+} = 16(1)\%$. FTIR investigations pointed to the occurrence of Fe^{3+}-oxy substitutions and ruled out the presence of vacancy mechanisms. The overall crystal-chemical features are consistent with the following substitutions: tetraferriphlogopite [$^{IV}Fe^{3+} \leftrightarrow {}^{IV}Al$]; Ti-oxy [$^{VI}M^{2+} + 2\ (OH)^- \leftrightarrow {}^{VI}Ti^{4+} + 2\ (O^{2-}) + H_2\uparrow$] and Al, Fe^{3+}, Cr-oxy [$^{VI}M^{2+} + (OH)^- \leftrightarrow {}^{VI}M^{3+} + O^{2-} + ½\ (H_2)\uparrow$]; Al, Fe^{3+}-Tschermak [$^{VI}M^{2+} + {}^{IV}Si^{4+} \leftrightarrow {}^{VI}M^{3+} + {}^{IV}Al$]; kinoshitalite [$^{XII}K + {}^{IV}Si^{4+} \leftrightarrow {}^{XII}Ba^{2+} + {}^{IV}Al$] and [$^{XII}K^+ + {}^{IV}Al^{3+} \leftrightarrow {}^{IV}Si^{4+} + {}^{XII}\square$].

The estimation of the OH^- content for Ugandan mica-2M_1 was obtained, for the first time, from the linear regression equation $c = 0.20(2) \times OH^-$ (gpfu) + 19.93(2) derived from literature data of 2M_1-samples with known OH^- content. The orientation of the O-H vector with respect to **c*** was found in the range from 2.0 to 6.9°.

Keywords: Kamafugitic 2M_1-phlogopites, crystal chemistry, substitution mechanisms, Mössbauer, FTIR

Introduction

It is known that the mica structure arises from the stacking of T-O-T layers along the *c*-axis direction connected by I-cations where T, O, and I stand for tetrahedral-, octahedral-, and interlayer, respectively. The six standard mica polytypes, 1*M*, 2M_1, 2M_2, 2*O*, 3*T*, and 6*H*, theoretically derived by Smith and Yoder (1956), were subsequently classified on the basis of the mutual rotation between the two neighboring T-O-T layers, into three types: (1) subfamily A (1*M*, 2M_1, and 3*T*), with successive layers rotated by $2n \times 60°$; (2) subfamily B (2M_2, 2*O*, and 6*H*) with successive layers rotated by $(2n + 1) \times 60°$; and (3) mixed polytypes in which both types A and B occur (Nespolo 1999).

In trioctahedral micas, polytype 2M_1 occurs less frequently than the 1*M* polytype (Bailey 1984a). For this reason, the trioctahedral 1*M*-polytype has been extensively studied to date, whereas studies on the 2M_1-polytype are relatively scarce.

In several cases, 2M_1-micas have been reported as coexisting with 1*M*-micas in the same rock sample. Takeda and Ross (1975), analyzed 2M_1 and 1*M* igneous oxybiotite from Ruiz Peak (New Mexico), and concluded that the unit layer of the 2M_1 polytype showed a shift of the upper and lower triads of octahedral O atoms along the $\pm b$ direction with respect to the 1*M* polytype. This caused the reduction in the unit layer symmetry from *C*2/*m* to $C\bar{1}$.

Bohlen et al. (1980) carried out a full crystal-chemical characterization of a metamorphic 2M_1 biotite from Au Sable Forks, New York, and concluded that chemistry and structure were quite close to the Ruiz Peak specimen of Takeda and Ross (1975). Ohta et al. (1982) studied hydrogenated and hydrogen-depleted Fe^{3+}-rich 1*M* and 2M_1 igneous biotites from Ruiz Peak. The lack of hydrogen seemed to mainly affect the interlayer configuration, causing a decrease in the interlayer separation.

2M_1- and 1*M*-micas in plutonic rocks from Valle del Cervo and in ignimbrites and lavas from Mt. Sassetto, Italy, were studied by Bigi and Brigatti (1994) and Laurora et al. (2007), respectively. By comparing the two polytypic forms, Bigi and Brigatti (1994) concluded that, despite the similarity in the chemical composition, the 2M_1 polytype had the most pronounced tetrahedral and octahedral distortions. Laurora et al. (2007) found that the 2M_1 polytype had structural features compatible with the occurrence of Ti-oxy substitutions. Aldega et al. (2009) reported, through X-ray powder diffraction, the coexistence of 1*M*- and 2M_1-polytypes in phlogopite from altered volcanoclastic deposits in the Grotta del Cervo cave, Pietrasecca, Italy.

Other studies focused on the characterization of phlogopite-annite 2M_1 micas with peculiar composition. For instance, Bigi et al. (1993) analyzed crystals from diorites with high Ti and ^{XII}Ba content. The authors associated the decrement of the tetrahedral layer thickness to the entrance of ^{XII}Ba by means of the $^{IV}Si + {}^{XII}K \leftrightarrow {}^{IV}Al + {}^{XII}Ba$ substitution mechanism. Brigatti et al. (2000) investigated a 2M_1, Al-rich biotite from a pluton of Northern

* E-mail: f.scordari@geomin.uniba.it

0003-004X/12/0203–430$05.00/DOI: http://dx.doi.org/10.2138/am.2012.3896

Victoria Land (Antarctica) showing a preferential partitioning of the Al in the octahedral M2 site and a disordered distribution of Fe and Mg between the M1 and M2 sites. Brigatti et al. (2005) studied a magnesian annite-2M_1, high in Fe, Ti, and F, and low in Ba, sampled from the youngest unit of the volcanic sequences detected at the Albano maar lake. The authors observed that the geometry of the M1 octahedra was mainly influenced by the Fe content. Another 2M_1 magnesian annite from granitic rocks of Oquossoc, western Maine, showed tetraferri-phlogopite component (Brigatti et al. 2008). In this sample, the large individual T-O3 distances were explained in part by the tetrahedral chemical composition and in part by the cation ordering between the octahedral M1 and M2 sites. In a very recent work, the crystal chemistry and the magnetic behavior of a Fe^{2+}-rich 2M_1 mica from Minto Block in the northern Quebec was reported (Pini et al. 2008). The authors derived Fe^{2+} preferential partitioning into the M1 site by the crystal structure refinement and XAS analysis.

Finally, several studies have been devoted to 2M_1 micas with remarkably rare compositions and/or cation ordering, causing their symmetry to lower from *C*2/*c* to *Cc* (i.e., Lahti and Saikkonen 1985; Slade and Radoslovich 1985; Rieder et al. 1996), *C*1 (Slade et al. 1987), or to *Am* (Bujnowski et al. 2009).

In the present paper, a phlogopite specimen from Bunyaruguru kamafugite (south west Uganda, west branch of the East African Rift) shows, for the first time, only the 2M_1 polytype. The phlogopite has been investigated by a multi-analytical approach, consisting of a combination of electron probe microanalysis (EPMA), single-crystal X-ray diffraction (SCXRD), and Mössbauer and Fourier transform infrared (FTIR) spectroscopy. To the best of our knowledge, this is the first integrated crystal chemical study of phlogopite from Ugandan kamafugites, and it was undertaken to gain insight into the crystal chemistry of the trioctahedral mica 2M_1-polytype. Thus far, these phlogopites have been investigated only by means of chemical analyses (Lloyd et al. 1999; Mugnai 2003; Tappe et al. 2003; Murav'eva and Senin 2009).

Materials and methods

Samples

Mica crystals studied here were separated from a Ugandan kamafugitic rock, labeled "BU3" rock, petrographically characterized elsewhere (Mugnai 2003; Stoppa et al. 2003). In brief, the BU3 rock is a tuffisite from Kichwamba (Bunyaruguru field) and has a modal mineralogy consisting of 15% phlogopite, 25% melilite, 15% clinopyroxene, 15% olivine, 10% perovskite, and 20% carbonates (Mugnai 2003; Stoppa et al. 2003). Only 2M_1-micas have been found in the BU3 rock. Mica crystals were given the same labels as their host rock.

EPMA

Major element analyses of the phlogopites were obtained by a JEOL JXA-8200 electron microprobe using the following operating conditions: 15 kV accelerating voltage, 5 nA sample current, ~1 μm spot size, 40 s counting time. Wavelength-dispersive spectrometry (WDS) mode for F, Na, K, Ba, Ca, Cl, Ti, Cr, Mn, Ni, Sr, Zn, and Zr, and energy-dispersive spectrometry (EDS) mode for Si, Al, Mg, and Fe were used. The following standards were used: grossular (Si-Al), olivine (Mg), omphacite (Na), ilmenite (Ti), rhodonite (Mn), K-feldspar (K), Cr pure (Cr), fayalite (Fe), wollastonite (Ca), sanbornite (Ba), apatite (F), celestine (Sr), nickeline (Ni), scapolite (Cl), rhodonite (Zn), and zircon (Zr). Raw data were corrected using the Phi-Rho-Z method as implemented in the JEOL suite of programs.

The analyses were carried out on 5 single crystals that were also evaluated by structure refinement. Five point analyses were performed on each crystal to test for chemical homogeneity. Average oxide weight percents are reported in Table 1, whereas a classification plot of the compared micas is shown in Figure 1.

Mössbauer spectroscopy

^{57}Fe Mössbauer spectra were acquired on 512 channels using a conventional Mössbauer apparatus with a ^{57}Co/Rh single-line thin-source. Measurements were conducted by transmission in constant acceleration mode over a Doppler velocity range of ±4 mm/s. The data collected were folded to give a flat background and a zero-velocity position corresponding to the center shift of metallic α-Fe at room temperature (RT).

The Mössbauer spectrum of the BU3 phlogopite was recorded from about 9 mg of powdered sample obtained by crushing the mica under acetone to minimize oxidation by atmospheric oxygen. For the fitting of the spectrum, the Voigt-based Quadrupole Splitting Distribution (QSD) method developed by Rancourt and Ping (1991) and implemented in the software RECOIL was used (Lagarec and Rancourt 1997, 1998). The results of the RT Mössbauer investigation are shown in Table 2 and Figure 2.

Table 1. Electron microprobe data (wt%) of the studied phlogopite

	BU3_1	BU3_2	BU3_6	BU3_10	BU3_12
SiO_2	39.6(2)	39.3(3)	39.7(3)	39.1(2)	40.4(2)
Al_2O_3	12.8(2)	12.3(1)	12.9(2)	12.3(1)	12.70(8)
MgO	20.3(2)	19.3(1)	20.4(2)	17.9(1)	18.3(3)
FeO	6.5(2)	6.59(9)	6.5(1)	9.2(1)	9.0(2)
TiO_2	5.70(7)	5.82(9)	5.8(2)	7.05(9)	6.88(9)
Cr_2O_3	0.35(2)	0.34(4)	0.32(4)	0.02(1)	0.02(1)
NiO	0.06(5)	0.08(2)	0.08(3)	0.02(1)	0.06(1)
MnO	0.04(3)	0.03(1)	0.07(3)	0.06(1)	0.06(1)
SrO	0.03(3)	0.04(6)	0.03(4)	0.00(1)	0.03(4)
ZnO	0.01(1)	0.00(1)	0.00(1)	0.00(1)	0.08(6)
ZrO_2	0.01(2)	0.01(1)	0.03(2)	0.00(1)	0.01(0)
K_2O	10.00(2)	9.82(9)	9.98(7)	9.87(7)	9.73(7)
Na_2O	0.33(4)	0.30(3)	0.31(3)	0.30(4)	0.32(2)
BaO	0.29(6)	0.34(5)	0.27(4)	0.21(4)	0.28(5)
CaO	b.d.l.	0.00(1)	b.d.l.	0.00(1)	0.10(8)
F	0.07(5)	0.09(7)	0.08(3)	0.08(3)	0.06(2)
Cl	0.01(1)	0.01(1)	0.01(1)	0.01(0)	0.01(0)
Total	96.1(4)	94.4(1)	96.5(8)	96.1(5)	98.0(6)

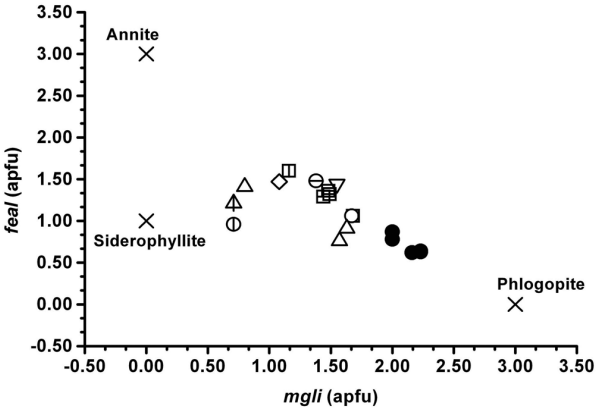

Figure 1. *Feal* vs. *mgli* diagram modified after Tischendorf et al. (2004). *Feal* and *mgli* stand, respectively, for (Fe_{tot}+Mn+Ti-^{VI}Al) and (Mg-Li). For comparison, all other trioctahedral 2M_1 micas with a composition ranging between the phlogopite-annite end-members from the literature are included. Symbols: Solid symbols = volcanic phlogopites of this work (circle: BU3); open symbols = igneous phlogopites from literature (square: Takeda and Ross 1975; circle: Ohta et al. 1982; pointing upward triangle: Bigi et al. 1993; pointing downward triangle: Bigi and Brigatti 1994; diamond: Brigatti et al. 2005); open symbols with horizontal line = other igneous phlogopites from literature (square: Laurora et al. 2007; circle: Pini et al. 2008); open symbols with vertical line = metamorphic phlogopites from literature (square: Bohlen et al. 1980; circle: Brigatti et al. 2000; pointing upward triangle: Brigatti et al. 2008).

SCXRD

A preliminary check on more than 40 crystals showed that in the studied sample only the $2M_1$ polytype was formed. For X-ray diffraction measurements, a Bruker AXS X8 APEXII automated diffractometer equipped with a four-circle Kappa goniometer, a CCD detector, and monochromatized Mo$K\alpha$ radiation was used. Operating conditions were 50 kV, 30 mA, and a crystal-to-detector distance of 40 mm. Data collection was optimized by the Apex program suite (Bruker 2003a) and the entire Ewald sphere ($\pm h, \pm k, \pm l$) was recorded by a combination of several ω and ϕ rotation sets, with 1.0° scan width and at least 10 s per frame exposure time. The SAINT package was used for the extraction of the reflection intensities and for the correction of the Lorentz-polarization (Bruker 2003b) and the SADABS software was used for a semi-empirical absorption correction (Sheldrick 2003). The structure refinements were performed in space group *C*2/*c* using the program CRYSTALS (Betteridge et al. 2003) starting from the atomic coordinates of Quebec biotite (Pini et al. 2008). Reflections with $I > 3\sigma(I)$ were considered as observed and the refined parameters were: scale factor, atomic positions, cation occupancies, and anisotropic atomic displacement parameters. For each crystal, with the exception of BU3_12, the difference-Fourier maps revealed a peak located at the expected position for the hydrogen atom (at about 0.80 Å from the O4 oxygen). After the inclusion of the H atom in the last cycles of the refinements, the final difference-Fourier maps became featureless. The unit-cell parameters and experimental details are reported in Table 3. Table 4 lists the final atomic coordinates, site occupancies, and isotropic and anisotropic displacement parameters. Relevant cation-anion bond lengths, selected geometrical parameters, mean atomic numbers and mean distances (as determined by structure refinement and chemical determinations) are given in Tables 5, 6, and 7, respectively.

FTIR

The infrared spectra were collected over the range 4000–550 cm^{-1} using a Nicolet Avatar FTIR spectrometer with a nominal resolution of 4 cm^{-1}, equipped with a Continuμm microscope, a MCT nitrogen-cooled detector, and a KBr beamsplitter. The measurements were performed on single crystals mounted on glass capillaries and laid down on the cleavage plane. The observed IR-patterns resulted from the average of 128 scans. The OH-stretching region (3750−3600 cm^{-1}) was modeled using the program PeakFit (Jandel Scientific), assuming Gaussian functions to describe the peaks and a linear function to approximate the background. Band positions and assignments (see details in section Hydrogen speciation below) are given in Table 8 and Figure 3.

TABLE 2. Mössbauer parameters of BU3 phlogopite as obtained by the QSD fitting method

	χ^2_r	Species	δ_0‡ (mm/s)	A^-/A^+	ΔE_Q (mm/s)	σ	P (%)	A (%)
		$^{VI}Fe^{2+}$	1.1(1)	1*	2.4(2)	0.30(2)	80*	60(1)
					2.3(3)	0.8(3)	20*	
BU3	1.2	$^{VI}Fe^{3+}$	0.4(3)	1*	1.0(5)	0.33(4)	100*	24(1)
		$^{IV}Fe^{3+}$	0.2*	1*	0.37(9)	0.3*	100*	16(1)

Notes: χ^2_r = reduced χ^2 = χ^2/degrees of freedom; $\delta = \delta_0 + \delta_1 \Delta E_Q$, $\delta_1 = 0$ during fitting; A^-/A^+ = ratio between low- and high-velocity spectral areas of the Mössbauer doublets; ΔEQ = quadrupole splitting and position of the individual Gaussian component to the QSD; σ = width of the individual Gaussian component to the QSD; P = portion of the individual Gaussian component to the QSD. * Fixed parameters.

RESULTS

Chemical analyses

Among major components, the main chemical variation in the studied crystals is relevant to MgO [17.9(1)–20.4(2) wt%], FeO [6.5(2)–9.2(1) wt%], and TiO_2 [5.70(7)–7.05(9) wt%, see Table 1].

In general, the BU3 crystals are Ti-rich, F-poor phlogopites and have a low annitic component, $Fe_{tot}/(Fe_{tot} + Mg)$, which ranges from 0.15 to 0.22. Figure 1 shows that they cluster along the annite-phlogopite join, very close to the phlogopite end-member [*mgli* ~ 2.1 atoms per formula unit (apfu) and *feal* ~ 0.7 apfu], whereas the literature $2M_1$-micas fall within the range $0.7 \le mgli \le 1.7$ and $0.8 \le feal \le 1.6$. Note that some samples (see phlogopites from Brigatti et al. 2000, 2008) approach the siderophyllite end-member owing to relatively high-Al contents. Therefore, in contrast to the literature data, in which $2M_1$-micas are Mg-rich annites, the crystals of this work can be classified as Fe^{2+}-rich phlogopite.

Structure refinements

The refined unit-cell parameters of the $2M_1$ phlogopites studied here are within the range: $5.3252(1) \le a \le 5.3307(1)$, $9.2231(3) \le b \le 9.2315(3)$, $20.1550(6) \le c \le 20.1964(8)$ Å, and $94.994(2) \le \beta \le 95.131(2)°$.

Compared to the literature data, the BU3 crystals lattice parameters lie between those of the $2M_1$ Ruiz Peak oxybiotite [a = 5.3175(7), b = 9.212(2), c = 19.976(3) Å, and β = 95.09(1)° (Ohta et al. 1982)] and those of the $2M_1$ magnesian annite from granitic rocks of Oquossoc [a = 5.374(3), b = 9.300(3), c = 20.317(8) Å, and β = 95.13(3)° (Brigatti et al. 2008)].

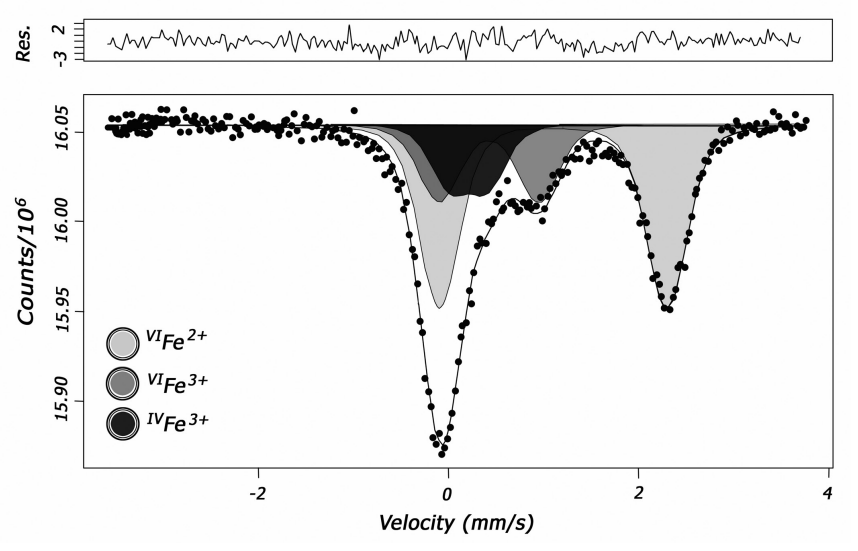

FIGURE 2. Transmission ^{57}Fe Mössbauer spectrum for BU3 phlogopite.

TABLE 3. Crystal, experimental, and refinement data of the studied micas

	BU3_1	BU3_2	BU3_6	BU3_10	BU3_12
Crystal size (mm³)	0.68 × 0.95 × 0.05	0.50 × 0.49 × 0.04	0.71 × 0.41 × 0.03	0.62 × 0.55 × 0.04	0.41 × 0.15 × 0.01
Space group	*C*2/*c*	*C*2/*c*	*C*2/*c*	*C*2/*c*	*C*2/*c*
a (Å)	5.3273(2)	5.3255(2)	5.3252(1)	5.3283(2)	5.3307(1)
b (Å)	9.2231(3)	9.2285(4)	9.2246(2)	9.2304(3)	9.2315(3)
c (Å)	20.1964(8)	20.1897(8)	20.1908(3)	20.1565(6)	20.1550(6)
β	95.121(2)	94.994(2)	95.086(1)	95.131(2)	95.095(2)
Cell volume (Å³)	988.37(6)	988.48(7)	987.40(5)	987.37(5)	987.92(5)
Z	4	4	4	4	4
θ range for data collection	2 to 42°	2 to 45°	2 to 45°	2 to 45°	4 to 39°
Reflections collected	29357	33714	59187	56205	14015
Reflections unique	3266	4055	3993	3810	2800
$R_{merging}$ [$R_{(int)}$] (%)	4.27	3.67	3.65	4.31	3.54
Reflections used					
$I > 3\sigma(I)$	2168	2532	2373	2155	1394
No. of refined parameters	110	110	110	110	106
Goof*	1.078	1.040	1.022	0.993	0.982
R_1† [on F] (%)	3.52	2.92	2.77	3.44	2.91
wR_2‡ [on F^2] (%)	3.89	3.08	3.04	4.02	2.91
$\Delta\rho_{min}/\Delta\rho_{max}$ (e/Å³)	–0.85/0.74	–0.85/0.83	–0.51/0.73	–0.92/0.90	–0.54/0.91

* Goodness-of-fit = $[\Sigma[w(F_o^2 - F_c^2)^2]/(N\text{-}P)]^{1/2}$, where N and P are the number of reflections and parameters, respectively.
† $R_1 = \Sigma[|F_o| - |F_c|]/\Sigma|F_o|$.
‡ $wR_2 = \{\Sigma[w(F_o^2 - F_c^2)^2]/\Sigma[w(F_o^2)^2]\}^{1/2}$; w = Chebychev optimized weights.

TABLE 4. Crystallographic coordinates, site occupancies, equivalent/isotropic (Å²), and anisotropic displacement parameters (Å²) of the studied micas

Site	Atom	*x*	*y*	*z*	Occupancy	$U_{iso/equiv}$	U_{11}	U_{22}	U_{33}	U_{23}	U_{13}	U_{12}
Sample BU3_1												
K	K^+	0	0.08384(8)	¼	1.005(2)	0.0354	0.0351(3)	0.0327(3)	0.0384(3)	0	0.0033(2)	0
M1	Mg^{2+}	¾	¼	0	0.813(3)	0.0116	0.0107(2)	0.0079(2)	0.0165(2)	–0.0020(2)	0.0019(2)	–0.0072(2)
	Fe^{2+}	¾	¼	0	0.187(2)	0.0116	0.0107(2)	0.0079(2)	0.0165(2)	–0.0020(2)	0.0019(2)	–0.0072(2)
M2	Mg^{2+}	0.24271(7)	0.08080(4)	0.00002(2)	0.79(2)	0.0140	0.0175(2)	0.0096(2)	0.0147(2)	–0.0009(1)	0.0010(1)	0.0118(1)
	Fe^{2+}	0.24271(7)	0.08080(4)	0.00002(2)	0.219(9)	0.0140	0.0175(2)	0.0096(2)	0.0147(2)	–0.0009(1)	0.0010(1)	0.0118(1)
T1	Si, Si^{4+}	0.46198(7)	0.24996(4)	0.13693(2)	1.00(5)	0.0105	0.0100(1)	0.0071(1)	0.0144(1)	–0.0001(1)	0.0015(1)	0.0014(1)
T2	Si, Si^{4+}	0.96296(7)	0.41697(4)	0.13687(2)	1.00(6)	0.0113	0.0117(1)	0.0080(1)	0.0143(1)	0.0000(1)	0.0013(1)	0.0021(1)
O11	O, O^{2-}	0.7414(2)	0.3142(1)	0.16543(6)	1.00(6)	0.0199	0.0184(5)	0.0236(5)	0.0177(4)	0.0018(4)	0.0007(3)	–0.0060(4)
O21	O, O^{2-}	0.2412(2)	0.3526(1)	0.16592(6)	1.00(7)	0.0196	0.0191(5)	0.0217(5)	0.0179(4)	–0.0017(4)	0.0003(3)	0.0068(4)
O22	O, O^{2-}	0.4340(2)	0.0836(1)	0.16589(6)	1.00(7)	0.0192	0.0279(5)	0.0120(4)	0.0183(4)	0.0001(3)	0.0049(3)	0.0016(4)
O31	O, O^{2-}	0.4328(2)	0.2494(1)	0.05446(5)	1.00(6)	0.0119	0.0123(4)	0.0091(3)	0.0145(3)	–0.0004(3)	0.0015(3)	0.0044(3)
O32	O, O^{2-}	0.9366(2)	0.4174(1)	0.05442(5)	1.00(6)	0.0118	0.0122(3)	0.0092(3)	0.0142(3)	–0.0004(3)	0.0015(3)	0.0046(3)
O4	O, O^{2-}	0.9345(2)	0.0821(1)	0.05074(5)	1.00(7)	0.0133	0.0163(4)	0.0106(3)	0.0130(3)	–0.0007(3)	0.0008(3)	0.0065(3)
	H	0.945(1)	0.085(6)	0.088(3)	0.46(6)	0.0133	0.0163(4)	0.0106(3)	0.0130(3)	–0.0007(3)	0.0008(3)	0.0065(3)
Sample BU3_2												
K	K^+	0	0.08367(7)	¼	1.002(2)	0.0347	0.0334(2)	0.0343(3)	0.0364(3)	0	0.0027(2)	0
M1	Mg^{2+}	¾	¼	0	0.808(2)	0.0109	0.0086(2)	0.0092(2)	0.0150(2)	–0.0004(2)	0.0015(1)	–0.0005(2)
	Fe^{2+}	¾	¼	0	0.192(2)	0.0109	0.0086(2)	0.0092(2)	0.0150(2)	–0.0004(2)	0.0015(1)	–0.0005(2)
M2	Mg^{2+}	0.24315(5)	0.08106(3)	0.00001(1)	0.775(3)	0.0125	0.0142(1)	0.0100(1)	0.0133(1)	0.0006(2)	0.00065(8)	0.0037(1)
	Fe^{2+}	0.24315(5)	0.08106(3)	0.00001(1)	0.225(2)	0.0125	0.0142(1)	0.0100(1)	0.0133(1)	0.0006(2)	0.00065(8)	0.0037(1)
T1	Si, Si^{4+}	0.46204(5)	0.25008(3)	0.13692(1)	1.000(7)	0.0097	0.00825(8)	0.00843(9)	0.01235(9)	–0.00023(9)	0.00086(7)	–0.00040(9)
T2	Si, Si^{4+}	0.96285(5)	0.41699(4)	0.13687(1)	1.000(7)	0.0106	0.00950(9)	0.00987(9)	0.01248(9)	–0.0004(1)	0.00083(7)	–0.0006(1)
O11	O, O^{2-}	0.7416(2)	0.3143(1)	0.16528(5)	1.000(7)	0.0194	0.0173(3)	0.0247(4)	0.0159(3)	0.0022(3)	0.0000(3)	–0.0068(3)
O21	O, O^{2-}	0.2412(2)	0.3526(1)	0.16595(5)	1.000(7)	0.0190	0.0159(3)	0.0240(4)	0.0170(3)	–0.0025(3)	–0.0004(3)	0.0055(3)
O22	O, O^{2-}	0.4338(2)	0.0834(1)	0.16590(4)	1.000(7)	0.0191	0.0282(4)	0.0132(3)	0.0164(3)	0.0003(3)	0.0040(3)	0.0003(3)
O31	O, O^{2-}	0.4329(1)	0.25818(9)	0.05437(4)	1.000(7)	0.0090	0.0104(2)	0.0040(2)	0.0127(2)	–0.0023(2)	0.0010(2)	0.0003(2)
O32	O, O^{2-}	0.9363(1)	0.42577(9)	0.05429(3)	1.000(7)	0.0084	0.0098(2)	0.0033(2)	0.0120(2)	–0.0017(2)	0.0009(2)	–0.0005(2)
O4	O, O^{2-}	0.9347(1)	0.09149(9)	0.05091(4)	1.000(7)	0.0104	0.0128(2)	0.0057(2)	0.0126(2)	0.0028(2)	0.0007(2)	0.0007(2)
	H	0.946(6)	0.090(4)	0.089(2)	0.561(7)	0.0104	0.0128(2)	0.0057(2)	0.0126(2)	0.0028(2)	0.0007(2)	0.0007(2)
Sample BU3_6												
K	K^+	0	0.08381(7)	¼	0.992(2)	0.0329	0.0324(2)	0.0320(3)	0.0344(3)	0	0.0029(2)	0
M1	Mg^{2+}	¾	¼	0	0.809(2)	0.0094	0.0077(2)	0.0071(2)	0.0136(2)	–0.0005(2)	0.0017(1)	–0.0017(2)
	Fe^{2+}	¾	¼	0	0.191(2)	0.0094	0.0077(2)	0.0071(2)	0.0136(2)	–0.0005(2)	0.0017(1)	–0.0017(2)
M2	Mg^{2+}	0.24315(5)	0.08098(3)	0.00000(1)	0.776(3)	0.0112	0.0132(1)	0.0085(1)	0.0118(1)	0.0010(2)	0.00090(8)	0.0026(2)
	Fe^{2+}	0.24315(5)	0.08098(3)	0.00000(1)	0.224(2)	0.0112	0.0132(1)	0.0085(1)	0.0118(1)	0.0010(2)	0.00090(8)	0.0026(2)
T1	Si, Si^{4+}	0.46198(6)	0.25002(4)	0.13689(2)	1.000(7)	0.0085	0.00767(9)	0.00704(9)	0.0110(1)	–0.0002(1)	0.00098(7)	–0.00022(9)
T2	Si, Si^{4+}	0.96289(5)	0.41689(4)	0.13688(1)	1.000(7)	0.0089	0.00819(9)	0.00765(9)	0.01085(9)	–0.0003(1)	0.00097(7)	–0.0005(1)
O11	O, O^{2-}	0.7412(2)	0.3144(1)	0.16533(5)	1.000(7)	0.0178	0.0164(4)	0.0230(4)	0.0137(3)	0.0021(3)	0.0001(3)	–0.0062(3)
O21	O, O^{2-}	0.2411(2)	0.3524(1)	0.16596(5)	1.000(7)	0.0178	0.0157(4)	0.0222(4)	0.0150(3)	–0.0021(3)	–0.0003(3)	0.0061(3)
O22	O, O^{2-}	0.4342(2)	0.0834(1)	0.16587(4)	1.000(7)	0.0176	0.0268(4)	0.0117(3)	0.0147(3)	0.0001(3)	0.0041(3)	0.0007(3)
O31	O, O^{2-}	0.4326(1)	0.25702(9)	0.05436(4)	1.000(7)	0.0080	0.0091(2)	0.0042(2)	0.0108(2)	–0.0015(2)	0.0013(2)	0.0005(2)
O32	O, O^{2-}	0.9364(1)	0.42469(9)	0.05438(4)	1.000(7)	0.0075	0.0089(2)	0.0030(2)	0.0107(2)	–0.0012(2)	0.0013(2)	–0.0003(2)
O4	O, O^{2-}	0.9348(1)	0.0903(1)	0.05094(4)	1.000(7)	0.0096	0.0116(2)	0.0059(2)	0.0112(2)	0.0034(3)	0.0009(2)	0.0008(3)
	H	0.939(7)	0.077(4)	0.095(2)	0.50(1)	0.0096	0.0116(2)	0.0059(2)	0.0112(2)	0.0034(3)	0.0009(2)	0.0008(3)

(Continued on next page)

TABLE 4.—*CONTINUED*

Site	Atom	*x*	*y*	*z*	Occupancy	$U_{iso/equiv}$	U_{11}	U_{22}	U_{33}	U_{23}	U_{13}	U_{12}
Sample BU3_10												
K	K^+	0	0.0839(1)	¼	0.992(2)	0.0350	0.0330(3)	0.0321(3)	0.0398(4)	0	0.0034(3)	0
M1	Mg^{2+}	¾	¼	0	0.726(3)	0.0114	0.0087(2)	0.0092(2)	0.0164(2)	–0.0008(2)	0.0021(2)	–0.0036(2)
	Fe^{2+}	¾	¼	0	0.274(2)	0.0114	0.0087(2)	0.0092(2)	0.0164(2)	–0.0008(2)	0.0021(2)	–0.0036(2)
M2	Mg^{2+}	0.24076(7)	0.08028(4)	0.00002(2)	0.722(3)	0.0126	0.0146(2)	0.0097(2)	0.0134(2)	0.0004(2)	0.0010(1)	0.0009(2)
	Fe^{2+}	0.24076(7)	0.08028(4)	0.00002(2)	0.278(3)	0.0126	0.0146(2)	0.0097(2)	0.0134(2)	0.0004(2)	0.0010(1)	0.0009(2)
T1	Si, Si^{4+}	0.46161(8)	0.24994(5)	0.13728(2)	1.000(7)	0.0100	0.0083(1)	0.0082(1)	0.0136(1)	0.0000(1)	0.0012(1)	0.0000(1)
T2	Si, Si^{4+}	0.96357(8)	0.41703(5)	0.13721(2)	1.000(7)	0.0108	0.0096(1)	0.0095(1)	0.0133(1)	0.0000(2)	0.0013(1)	0.0003(2)
O11	O, O^{2-}	0.7401(3)	0.3163(2)	0.16547(7)	1.000(7)	0.0195	0.0174(5)	0.0245(6)	0.0165(5)	0.0017(4)	0.0003(4)	–0.0067(4)
O21	O, O^{2-}	0.2387(3)	0.3504(2)	0.16637(7)	1.000(7)	0.0191	0.0167(5)	0.0231(6)	0.0173(5)	–0.0020(4)	0.0006(4)	0.0066(4)
O22	O, O^{2-}	0.4381(3)	0.0834(2)	0.16630(6)	1.000(7)	0.0193	0.0280(6)	0.0133(4)	0.0171(4)	0.0006(4)	0.0046(4)	0.0007(5)
O31	O, O^{2-}	0.4317(2)	0.2572(1)	0.05446(5)	1.000(7)	0.0099	0.0104(4)	0.0056(3)	0.0138(4)	–0.0014(3)	0.0013(3)	0.0004(3)
O32	O, O^{2-}	0.9370(2)	0.4253(1)	0.05450(5)	1.000(7)	0.0093	0.0101(3)	0.0048(3)	0.0130(3)	–0.0011(3)	0.0011(3)	–0.0011(3)
O4	O, O^{2-}	0.9349(2)	0.0904(1)	0.05094(5)	1.000(7)	0.0120	0.0139(4)	0.0083(3)	0.0138(3)	0.0035(4)	0.0016(3)	0.0005(4)
	H	0.947(9)	0.0099(5)	0.0905(5)	0.593(7)	0.0120	0.0139(4)	0.0083(3)	0.0138(3)	0.0035(4)	0.0016(3)	0.0005(4)
Sample BU3_12												
K	K^+	0	0.0840(1)	¼	1.0069(9)	0.0362	0.0337(4)	0.0328(4)	0.0420(4)	0	0.0032(3)	0
M1	Mg^{2+}	¾	¼	0	0.7288(8)	0.0119	0.0094(3)	0.0095(3)	0.0171(4)	0.0011(5)	0.0022(2)	0.0030(3)
	Fe^{2+}	¾	¼	0	0.2714(7)	0.0119	0.0094(3)	0.0095(3)	0.0171(4)	0.0011(5)	0.0022(2)	0.0030(3)
M2	Mg^{2+}	0.24036(9)	0.08007(6)	–0.00003(2)	0.6983(8)	0.0137	0.0157(2)	0.0107(2)	0.0147(2)	0.0026(5)	0.0010(2)	0.0077(3)
	Fe^{2+}	0.24036(9)	0.08007(6)	–0.00003(2)	0.3018(8)	0.0137	0.0157(2)	0.0107(2)	0.0147(2)	0.0026(5)	0.0010(2)	0.0077(3)
T1	Si, Si^{4+}	0.4620(1)	0.25017(6)	0.13724(3)	1.000(7)	0.0103	0.0084(2)	0.0083(2)	0.0142(2)	0.0006(3)	0.0013(2)	0.0016(2)
T2	Si, Si^{4+}	0.96326(9)	0.41742(8)	0.13725(3)	1.000(7)	0.0111	0.0102(2)	0.0096(2)	0.0136(2)	0.0008(3)	0.0012(1)	0.0028(3)
O11	O, O^{2-}	0.7395(3)	0.3164(2)	0.16557(9)	1.000(7)	0.0195	0.0179(7)	0.0231(8)	0.0174(7)	0.0020(6)	0.0011(6)	–0.0072(6)
O21	O, O^{2-}	0.2391(3)	0.3503(2)	0.16642(9)	1.000(7)	0.0199	0.0172(7)	0.0240(8)	0.0184(8)	–0.0019(7)	–0.0004(6)	0.0060(6)
O22	O, O^{2-}	0.4384(3)	0.0838(2)	0.16630(7)	1.000(7)	0.0196	0.0278(7)	0.0133(5)	0.0180(6)	–0.0001(7)	0.0044(5)	0.0013(7)
O31	O, O^{2-}	0.4321(2)	0.2408(2)	0.05452(7)	1.000(7)	0.0090	0.0106(5)	0.0028(5)	0.0138(6)	0.0017(5)	0.0015(5)	–0.0004(4)
O32	O, O^{2-}	0.9369(2)	0.4089(2)	0.05457(7)	1.000(7)	0.0097	0.0103(4)	0.0051(5)	0.0140(5)	0.0010(6)	0.0016(4)	0.0019(5)
O4	O, O^{2-}	0.9343(2)	0.0733(2)	0.05103(7)	1.000(7)	0.0102	0.0148(5)	0.0023(5)	0.0134(5)	–0.0021(5)	0.0007(4)	0.0013(5)

TABLE 5. Selected bond distances (Å) of the studied micas

	BU3_1	BU3_2	BU3_6	BU3_10	BU3_12
T1-O11	1.657(1)	1.6574(9)	1.656(1)	1.658(1)	1.655(2)
T1-O21	1.657(1)	1.6560(9)	1.656(1)	1.655(1)	1.654(2)
T1-O22	1.654(1)	1.657(1)	1.656(1)	1.653(1)	1.652(2)
T1-O31	1.659(1)	1.6620(8)	1.6611(8)	1.664(1)	1.663(2)
<T1-O>	1.657	1.658	1.657	1.658	1.656
T2-O11	1.657(1)	1.6534(9)	1.655(1)	1.651(1)	1.655(2)
T2-O21	1.655(1)	1.6563(9)	1.655(1)	1.649(1)	1.655(2)
T2-O22	1.657(1)	1.656(1)	1.656(1)	1.654(2)	1.654(2)
T2-O32	1.659(1)	1.6630(7)	1.6607(8)	1.662(1)	1.661(2)
<T2-O>	1.657	1.657	1.657	1.654	1.656
<T-O>	1.657	1.658	1.657	1.656	1.656
M1-O31(×2)	2.0972(9)	2.0941(7)	2.0963(7)	2.102(1)	2.102(1)
M1-O32(×2)	2.094(1)	2.1512(7)	2.1434(8)	2.150(1)	2.039(2)
M1-O4(×2)	2.058(1)	1.9970(8)	2.0046(8)	2.003(1)	2.121(2)
<M1-O>	2.083	2.081	2.081	2.085	2.087
M2-O31	2.087(1)	2.0261(8)	2.0326(9)	2.029(1)	2.063(2)
M2-O31′	2.110(1)	2.1692(8)	2.1593(9)	2.170(1)	2.147(2)
M2-O32	2.084(1)	2.0292(8)	2.0353(8)	2.035(1)	2.125(1)
M2-O32′	2.113(1)	2.1081(7)	2.1104(8)	2.120(1)	2.145(1)
M2-O4	2.007(1)	2.0146(8)	2.0152(8)	2.005(1)	1.938(2)
M2-O4′	2.011(1)	2.0782(9)	2.0684(9)	2.060(1)	2.005(1)
<M2-O>	2.069	2.071	2.070	2.070	2.071
<M-O>	2.074	2.074	2.074	2.075	2.076
K-O11(×2)	2.985(1)	2.990(1)	2.988(1)	3.000(2)	3.002(2)
K-O11′(×2)	3.339(1)	3.338(1)	3.338(1)	3.321(2)	3.318(2)
K-O21(×2)	2.986(1)	2.987(1)	2.987(1)	3.001(2)	3.002(2)
K-O21′(×2)	3.327(1)	3.327(1)	3.325(1)	3.300(2)	3.300(2)
K-O22(×2)	2.989(1)	2.9837(9)	2.9882(9)	3.000(1)	3.001(2)
K-O22′(×2)	3.326(1)	3.329(1)	3.325(1)	3.303(1)	3.303(2)
<K-O>inner	2.987	2.987	2.988	3.000	3.002
<K-O>outer	3.331	3.331	3.329	3.308	3.307
<K-O>	3.159	3.159	3.159	3.154	3.155
O-H	0.75(6)	0.76(3)	0.89(4)	0.80(1)	–

The <M1-O> distance (on average 2.083 Å) is significantly larger than the <M2-O> (on average 2.070 Å), pointing toward a meso-octahedral nature from a geometrical viewpoint (Weiss et al. 1985, 1992). However, they are homo-octahedral from a chemical viewpoint (Ďurovíč 1994), given that the maximum difference between M1 and M2 mean atomic numbers is ~0.5 e^- (see Table 7).

The observed variations in unit-cell parameters, interatomic distances, and octahedral mean atomic numbers confirm that the BU3 sample is characterized by low to moderate chemical variability, as highlighted in the Chemical analyses section. The largest differences in terms of structural parameters (i.e., *a*, *b*, and particularly the *c* lattice parameters, <M1-O>, $<K\text{-}O>_{inner}$, and $<K\text{-}O>_{outer}$ distances and distortion parameters) are illustrated by BU3_10 and BU3_12 crystals (see Tables 3, 5, and 6). The different structural parameters are likely related to the higher content of trivalent (Fe, ^{VI}Al) and tetravalent (Ti) cations in these crystals with respect to the others (see Table 9 and the Discussion section for further details).

In the examined samples, the O-H distance ranges from 0.75(6) to 0.89(4) Å. In addition, the O-H vector makes an angle with the **c*** axis in the range 2.0–6.9°.

Iron speciation

Three Fe-species were identified in the RT Mössbauer spectrum of the BU3 phlogopite: $^{VI}Fe^{2+}$, $^{VI}Fe^{3+}$, and $^{IV}Fe^{3+}$ (Fig. 2). The assignment and the values of the hyperfine parameters (center shifts, δ_o, and Quadrupole Splittings, ΔE_Q in Table 2) are in agreement with previous findings reported in the literature for trioctahedral micas (Rancourt et al. 1992, 1994a, 1994b, 1996; Redhammer 1998; Dyar 2002; Redhammer et al. 2005).

Hydrogen speciation

In Figure 3, the fitting of the OH^- stretching region in the FTIR spectrum of the BU3_2 crystal is shown. Similar spectra (not shown) were recorded for the other single crystals. The

spectrum consists of overlapping normal and impurity bands. Specifically, it is dominated by two broad and intense bands (A and C in Fig. 3) centered around 3710 and 3680 cm^{-1} that are unambiguously assigned to OH$^-$-K-OH$^-$ and OH$^-$-K-O^{2-} local arrangements, respectively, with MgMgMg as the octahedral cationic neighbors (see Libowitzky and Beran 2004; Scordari et al. 2006; Lacalamita et al. 2011). In addition, several shoulders shifted toward lower wavenumbers are present. The absorption band noted at about 3655 cm^{-1} (E band) is evidence of the occurrence of Fe^{3+}-oxy substitution mechanisms (Redhammer et al. 2000; Scordari et al. 2006; Lacalamita et al. 2011). Bands B and D centered at ~3695 and ~3670 cm^{-1}, respectively, can be assumed as a superposition of multiple components associated to hydroxyl groups vibrations (see Table 8 and Lacalamita 2009).

TABLE 6. Selected parameters derived from the structure refinements of the studied micas

	BU3_1	BU3_2	BU3_6	BU3_10	BU3_12
t_{tet} (Å)	2.264	2.263	2.262	2.263	2.263
BLD_{T1}	0.092	0.118	0.116	0.206	0.207
BLD_{T2}	0.060	0.176	0.128	0.245	0.167
V_{T1} (Å^3)	2.332	2.337	2.333	2.335	2.327
V_{T2} (Å^3)	2.333	2.332	2.330	2.320	2.328
TQE_{T1}	1.000	1.001	1.001	1.001	1.001
TQE_{T2}	1.000	1.002	1.002	1.005	1.001
TAV_{T1}	1.28	3.33	2.88	2.94	3.72
TAV_{T2}	1.38	3.38	2.96	3.12	3.86
τ_{T1} (°)	110.5	110.4	110.5	110.4	110.5
τ_{T2} (°)	110.5	110.5	110.5	110.5	110.5
α(°)	7.56	7.57	7.50	6.75	6.70
Δz (Å)	0.010	0.014	0.013	0.018	0.017
D.M. (Å)	0.510	0.507	0.505	0.491	0.487
ψ_{M1} (°)	59.08	59.06	59.05	59.13	59.12
ψ_{M2} (°)	58.84	58.90	58.86	58.87	58.84
BLD_{M1}	0.804	2.685	2.469	2.610	1.545
ELD_{M1}	5.214	5.126	5.132	5.218	5.157
BLD_{M2}	1.920	2.304	2.078	2.422	3.302
ELD_{M2}	4.932	4.906	4.890	4.885	4.839
$Shift_{M2}$ (Å)	0.062	0.057	0.058	0.078	0.082
V_{M1} (Å^3)	11.836	11.773	11.789	11.845	11.914
OQE_{M1}	1.012	1.014	1.014	1.015	1.013
OAV_{M1}	39.10	41.70	40.95	42.35	39.72
V_{M2} (Å^3)	11.610	11.639	11.633	11.620	11.620
OQE_{M2}	1.011	1.012	1.012	1.012	1.014
OAV_{M2}	36.10	37.50	36.76	37.64	38.86
$euM1/es_{M1}$	1.110	1.108	1.108	1.110	1.109
$euM2/es_{M2}$	1.104	1.103	1.103	1.103	1.102
t_{oct} (Å)	2.141	2.139	2.141	2.140	2.143
t_{int} (Å)	3.390	3.391	3.390	3.371	3.369
$\Delta_{K\text{-}O}$ (Å)	0.344	0.344	0.341	0.308	0.305
$t_{K\text{-}O4}$ (Å)	3.992	3.990	3.988	3.981	3.980

Notes: t_{tet} = tetrahedral sheet thickness calculated from z coordinates of basal and apical O atoms; TQE = tetrahedral quadratic elongation (Robinson et al. 1971); TAV = tetrahedral angle variance (Robinson et al. 1971); τ = tetrahedral flattening angle; α = tetrahedral rotation angle (Hazen and Burnham 1973); Δz = departure from coplanarity of the basal O atoms (Güven 1971); D.M. = dimensional misfit between tetrahedral and octahedral sheets (Toraya 1981); ψ = octahedral flattening angles (Donnay et al. 1964a, 1964b); BLD = bond-length distortions (Renner and Lehmann 1986); ELD = edge-length distortion (Renner and Lehmann 1986); $Shift_{M2}$ = off-center shift of the M2 cation defined as the distance between the M2 cation and ($X_{c,M2}$, $Y_{c,M2}$, $Z_{c,M2}$) where

$$X_{c,M2} = \frac{1}{6}\left(\sum_{i=0}^{6} X_{o,i}\right); Y_{c,M2} = \frac{1}{6}\left(\sum_{i=0}^{6} Y_{o,i}\right); Z_{c,M2} = \frac{1}{6}\left(\sum_{i=0}^{6} Z_{o,i}\right)$$

and the terms $X_{o,i}$, $Y_{o,i}$, $Z_{o,i}$ are a generic O atom defining M2 coordination (Laurora et al. 2007); OQE = octahedral quadratic elongation (Robinson et al. 1971); OAV = octahedral angle variance (Robinson et al. 1971); e_u, e_s = mean lengths of unshared and shared edges, respectively (Toraya 1981); t_{oct} = octahedral sheet thickness (Toraya 1981); t_{int} calculated from the z coordinates of basal O atoms; $\Delta_{K\text{-}O}$ = <K-O>$_{outer}$-<K-O>$_{inner}$; $t_{K\text{-}O4}$ = projection of K-O4 distance along **c***.

DISCUSSION

The structural formulas of the investigated samples (Table 9) were calculated on the basis of ($O_{12-x-y-z}OH_xCl_yF_z$) per formula unit by integrating the results from EPMA, SCXRD, Mössbauer spectrometry, and FTIR. In absence of direct H_2O measurements, the OH$^-$ content of each studied crystal was estimated from the equation $c = 0.20(2) \times OH^-$ (groups per formula unit, gpfu) + 19.93(2), $R^2 = 0.95$. The latter was obtained from linear regression analysis of the c vs. OH$^-$ content plot using 2M_1 phlogopites from the literature whose hydrogen content was directly determined (Fig. 4). Similar relationships have been previously proposed for 1M micas (see Cruciani and Zanazzi

TABLE 7. Mean atomic numbers (electron, e$^-$) of cation sites, octahedral and tetrahedral mean distances (Å) as determined by structure refinement (X-ref), and chemical determinations (EPMA) of the studied micas

	BU3_1	BU3_2	BU3_6	BU3_10	BU3_12
$e^-_{(M1)\ X\text{-}ref}$	14.62	14.69	14.67	15.84	15.80
$e^-_{(M2)\ X\text{-}ref}$	15.17	15.15	15.14	15.89	16.23
$e^-_{(M1+2M2)\ X\text{-}ref}$	44.96	44.99	44.95	47.62	48.26
$e^-_{(M1+2M2)\ EPMA}$	44.29	44.45	44.03	46.97	46.27
$K\ e^-_{X\text{-}ref}$	19.10	19.04	18.85	18.85	19.13
$K\ e^-_{EPMA}$	18.97	18.86	18.67	18.86	18.49
$T\ e^-_{X\text{-}ref}$	14.00	14.00	14.00	14.00	14.00
$T\ e^-_{EPMA}$	13.96	13.94	13.99	14.03	14.03
Σ^+_{EPMA}	22.77	22.82	22.75	22.98	22.97
Σ^-_{EPMA}	22.76	22.83	22.74	22.98	22.98
$<M\text{-}O>_{X\text{-}ref}$	2.074	2.074	2.074	2.075	2.076
$<M\text{-}O>_{EPMA}$	2.073	2.068	2.071	2.071	2.067
$<T\text{-}O>_{X\text{-}ref}$	1.657	1.658	1.657	1.656	1.656
$<T\text{-}O>_{EPMA}$	1.657	1.655	1.658	1.657	1.656

Notes: Average error for mean atomic numbers is ±0.5 e$^-$. Σ^+ and Σ^- are sum of positive and negative charges, respectively (see text for detail).

TABLE 8. Band position and assignment for the bands in the FTIR spectrum of the BU3_2 single crystal shown in Figure 3

Label	Position (cm^{-1})	Assignment
A	3709	MgMgMg-OH$^-$-K-OH$^-$
B	3696	MgMgFe^{2+}-OH$^-$-K-OH$^-$ + MgMgAl-OH$^-$-K- OH$^-$
C	3681	MgMgMg-OH$^-$-K-O^{2-}
D	3666	MgFe^{2+}Fe^{2+}-OH$^-$-K-OH$^-$ + MgMgFe^{3+}-OH$^-$-K-OH$^-$ + MgMgAl-OH$^-$-K-O^{2-}
E	3656	MgMgFe^{3+}-OH$^-$-K-O^{2-}
F	3640	not assigned

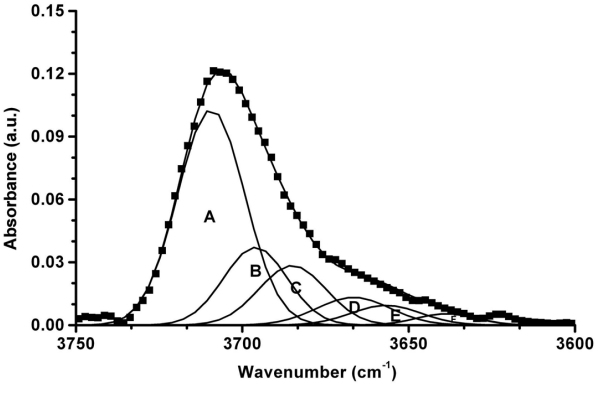

FIGURE 3. Fitting of the OH$^-$ stretching region in the FTIR spectrum of BU3_2 single crystal.

TABLE 9. Structural formulas of the studied micas

	Interlayer site	Octahedral site	Tetrahedral site	Anionic site
BU3_1	$(K_{0.94}Na_{0.05}Ba_{0.01})_{\Sigma=1.00}$	$(Mg_{2.23}Al_{0.09}Fe^{2+}_{0.24}Fe^{3+}_{0.10}Ti_{0.32}Cr0.02)_{\Sigma=3.00}$	$(Si_{2.91}Al_{1.02}Fe^{3+}_{0.07})_{\Sigma=4.00}$	$O_{10.76}F_{0.02}OH_{1.22}$
BU3_2	$(K_{0.94}Na_{0.04}Ba_{0.01})_{\Sigma=0.99}$	$(Mg_{2.16}Al_{0.13}Fe^{2+}_{0.25}Fe^{3+}_{0.10}Ti_{0.33}Cr0.02)_{\Sigma=2.99}$	$(Si_{2.96}Al_{0.96}Fe^{3+}_{0.07})_{\Sigma=3.99}$	$O_{10.83}F_{0.02}OH_{1.15}$
BU3_6	$(K_{0.93}Na_{0.04}Ba_{0.01})_{\Sigma=0.98}$	$(Mg_{2.23}Al_{0.09}Fe^{2+}_{0.24}Fe^{3+}_{0.09}Ti_{0.32}Cr0.02)_{\Sigma=2.99}$	$(Si_{2.91}Al_{1.03}Fe^{3+}_{0.07})_{\Sigma=4.01}$	$O_{10.74}F_{0.02}OH_{1.24}$
BU3_10	$(K_{0.94}Na_{0.04}Ba_{0.01})_{\Sigma=0.99}$	$(Mg_{2.00}Al_{0.11}Fe^{2+}_{0.35}Fe^{3+}_{0.14}Ti_{0.40})_{\Sigma=3.00}$	$(Si_{2.93}Al_{0.98}Fe^{3+}_{0.09})_{\Sigma=4.00}$	$O_{10.98}F_{0.02}OH_{1.00}$
BU3_12	$(K_{0.91}Na_{0.04}Ba_{0.01}Ca_{0.01})_{\Sigma=0.97}$	$(Mg_{2.00}Al_{0.15}Fe^{2+}_{0.33}Fe^{3+}_{0.13}Ti_{0.38})_{\Sigma=2.99}$	$(Si_{2.96}Al_{0.95}Fe^{3+}_{0.09})_{\Sigma=4.00}$	$O_{10.98}F_{0.01}OH_{1.01}$

1994; Ventruti et al. 2008).

The estimated OH^- contents for the 2M_1 Ugandan phlogopites of this work were varied within their standard deviations to obtain: (1) a full closure of the tetrahedral site taking into account that tetrahedral Fe^{3+} occurs, as substantiated by the Mössbauer spectroscopy (see Iron speciation section); (2) a fully occupied octahedral site, which is consistent with the absence of octahedral vacancies evidenced by the FTIR analyses (see Hydrogen speciation section); (3) a good agreement between X-ref and EPMA derived mean atomic numbers (see Table 7); and (4) a good match between <T-O> and <M-O> observed and calculated distances from ionic radii of Shannon (1976) (see Table 7). Slight differences in the octahedral composition allow one to cluster the BU3 phlogopite into two groups. Group 1 encompasses the BU3_1, BU3_2, and BU3_6 crystals, which have Mg ~2.20 apfu and Ti ~0.30 apfu. Group 2 includes the BU3_10 and BU3_12 crystals, which have Mg ~2.00 apfu and Ti ~0.40 apfu (Table 9). Group 1 and Group 2 phlogopites have also slightly different M1, M2 octahedral cation distributions. For instance, the single crystal BU3_1 (representative of Group 1) has the following distribution: $(Mg_{0.84}Fe^{2+}_{0.10}Fe^{3+}_{0.04}Cr_{0.02})$ at M1, $(Mg_{0.695}Fe^{2+}_{0.07}Fe^{3+}_{0.03}Ti_{0.16}Al_{0.045})$ at M2; the single-crystal BU3_10 (representative of Group 2) has the following distribution: $(Mg_{0.73}Fe^{2+}_{0.23}Fe^{3+}_{0.04})$ at M1, $(Mg_{0.635}Fe^{2+}_{0.06}Fe^{3+}_{0.05}Ti_{0.20}Al_{0.055})$ at M2. The above distributions are consistent with chemical and structural data. Note that Ti enters only the M2 site causing more pronounced distortions of the M2 octahedron compared to the M1 octahedron (see Tables 5 and 6), whereas Fe^{3+} is almost equally distributed over M1 and M2 sites.

The structural formulas of Table 9 are essentially balanced on the basis of the tetraferri-phlogopite [$^{IV}Fe^{3+} \leftrightarrow {}^{IV}Al$] and the Ti-oxy [$^{VI}M^{2+} + 2\,(OH)^- \leftrightarrow {}^{VI}Ti^{4+} + 2\,(O^{2-}) + H_2\uparrow$] substitution mechanisms. However, minor substitutions such as Al, Fe^{3+}, Cr-oxy [$^{VI}M^{2+} + OH^- \leftrightarrow {}^{VI}M^{3+} + O^{2-} + \frac{1}{2}\,(H_2)\uparrow$], Al, Fe^{3+}-Tschermak [$^{VI}M^{2+} + {}^{IV}Si^{4+} \leftrightarrow {}^{VI}(Al^{3+}, Fe^{3+}) + {}^{IV}Al^{3+}$], and those influencing the interlayer site, i.e., the kinoshitalite substitution [$^{XII}K^+ + {}^{IV}Si^{4+} \leftrightarrow {}^{XII}Ba^{2+} + {}^{IV}Al^{3+}$] and the [$^{XII}K^+ + {}^{IV}Al^{3+} \leftrightarrow {}^{IV}Si^{4+} + {}^{XII}\square$], also occur in the BU3 micas.

The tetraferri-phlogopite component found here has been documented only once in 2M_1 micas (see Brigatti et al. 2008). However, in BU3 phlogopite, the mean bond length <T-O> is significantly shorter [~1.657(1) Å, Table 5] than that found in tetraferri-phlogopite [1.669(3) Å] from Brigatti et al. (2008). This is consistent with higher Si (~2.93 vs. 2.78 apfu) and lower $^{IV}Fe^{3+}$ (~0.08 vs. 0.15 apfu) contents of the studied micas. Figure 5 shows that the average tetrahedral bond-length distortion ($<BLD>_T$) roughly increases with (^{IV}Al,$^{IV}Fe^{3+}$) for ^{IV}Si substitution. The BU3 micas exhibit the smallest bond-length tetrahedral distortions (average BLD_T ~0.15) over the whole data set, i.e., the most regular tetrahedra. Conversely, the tetraferri-phlogopite from Brigatti et al. (2008) is characterized by a high average BLD_T (0.73, Fig. 5) value. Given that no remarkable differences in the ^{IV}Al content exist between the two samples, it may be concluded that the $^{IV}Fe^{3+}$ emphasizes this tetrahedral distortion. In Figure 5, additional tetrahedral distortion in samples from Bigi et al. (1993) may be related to the high kinoshitalite component, which leads to a reduction in tetrahedral sheet thickness. In the same figure, the high tetrahedral distortion for the hydrogenated biotite of Takeda and Ross (1975) may be justified by the authors' argument involving symmetry lowering (from $C2/m$ to $C\bar{1}$) of the unit T-O-T layer in the 2M_1-polytype.

The T1 and T2 tetrahedral sites of the BU3 micas are not affected by cation ordering as indicated by the close similar-

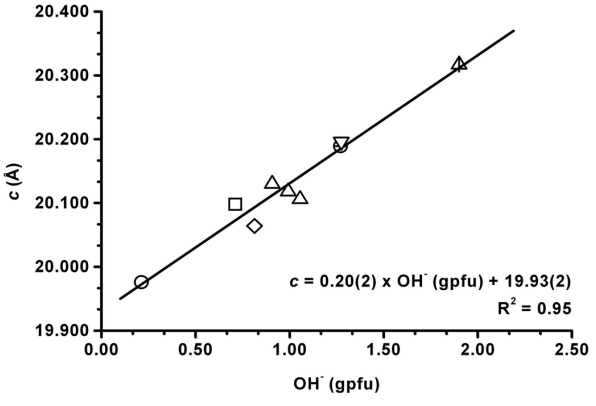

FIGURE 4. Plot of c cell parameter vs. OH^- groups per formula unit (gpfu.). Regression line on data from 2M_1 phlogopites of Takeda and Ross (1975), Ohta et al. (1982), Bigi et al. (1993), Bigi and Brigatti (1994), Brigatti et al. (2005, 2008), and Pini et al. (2008) is shown. Symbols as in Figure 1.

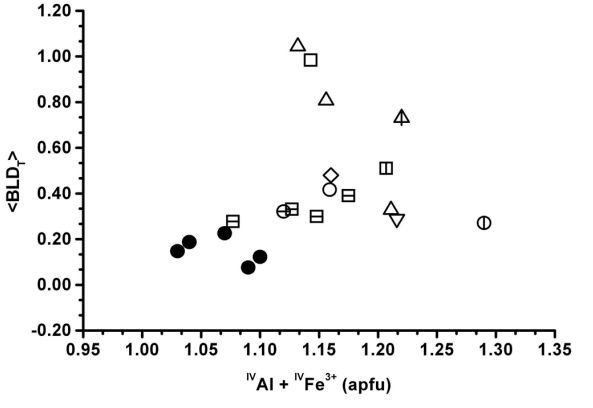

FIGURE 5. Plot of the average tetrahedral bond-length distortion parameter, $<BLD_T>$, vs. $^{IV}Al + {}^{IV}Fe^{3+}$ content. Symbols as in Figure 1.

ity between the <T1-O> and <T2-O> distances (Table 5) and confirmed by the TAV_{T1} vs. TAV_{T2} plot (Fig. 6).

In 1*M* micas, the entry of Ti via the oxy-type mechanism is reflected by the significant influence that it has on distinctive geometrical parameters, such as the *c* unit-cell parameter, M2-O4 distance, $shift_{M2}$, BLD_{M2}, K-O4 distance, $\Delta_{K\text{-}O}$, and t_{int} (Scordari et al. 2010a and references therein). For 2M_1 micas, these effects have not yet been systematically analyzed. In Figure 7, the BU3 phlogopites belonging to Group 1 are nearly superimposed in the plot and have $shift_{M2}$ parameter ~0.06 Å and Ti content ~0.30 apfu. On the other hand, BU3 phlogopites of Group 2 exhibit higher $shift_{M2}$ parameter (~0.08 Å) consistently with higher Ti content (~0.40 apfu).

Considering the whole data set a positive trend is found between the $shift_{M2}$ parameter and the Ti content. However, with the Ti content being almost equal (~0.35 apfu), a vertical spread of the $shift_{M2}$ values is observed, with the maximum value ($shift_{M2}$ ~0.15 Å) pertaining to the Ruiz Peak Fe^{3+}-oxybiotite of Ohta et al. (1982). This spread may indicate the coexistence of mechanisms enhancing the distortion due to the Ti-oxy substitution (for instance Fe^{3+}-oxy mechanisms). This is more clearly shown in Figure 8. It is known that the Ti-oxy mechanism is associated with deprotonation of the O4 oxygen atom, and that it influences the interlayer topology causing a decrease in the K-O4 distance and an increase in the K-O4 coulombic attraction (see Schingaro et al. 2011 and references therein). In Figure 8, the expected trend is confirmed for 2M_1 micas. Again, for the Ruiz Peak oxybiotite of Ohta et al. (1982), the reduction of the interlayer separation (t_{int} parameter) is greatly enhanced by the presence of substantial Fe^{3+}-oxy substitutions. This must be true also for the Mt. Sassetto biotite of Laurora et al. (2007), the magnesian annite of Brigatti et al. (2005), and the Ruiz Peak hydrogenated oxybiotite of Takeda and Ross (1975) even if no direct determination of Fe^{3+} was carried out by these authors. Note that the Al-rich biotite of Brigatti et al. (2000) and the tetraferriphlogopite of Brigatti et al. (2008) have the largest interlayer separation (Fig. 8). This is due to a notable degree of hydrogenation of these samples, which leads to remarkable H^+-K^+ coulombic repulsion.

The role of hydrogen in 2M_1 micas has not been widely investigated (Takeda and Ross 1975; Ohta et al. 1982; Slade et al. 1987; this work). It is known that, in trioctahedral micas, the O-H vector is nearly vertical to the (001) plane (Bailey 1984b, 1984c) and that there is a correlation between cation distribution and hydroxyl orientation (Giese 1979). However, in the case of the Ruiz Peak oxybiotite, Ohta et al. (1982) postulated that, in 2M_1 micas, due to the anisotropic repulsion forces acting on the hydrogen atom by the second and third nearest neighbor cations, the O-H axis should be tilted toward the *b* axis, i.e., away from the position directly under the interlayer K atom. In the present work, the position of the hydrogen has been refined for the 2M_1 micas under study. It was found that the O-H vector is nearly parallel to the **c*** axis. This result is in contrast with the conclusions by Ohta et al. (1982) concerning oxybiotites, but in agreement with the results of a structure refinement of ephesite-2M_1 (Slade et al. 1987). Despite the lower symmetry (space group *C*1) due to tetrahedral cation ordering, hydrogen refinement in the ephesite-2M_1 structure evidenced an average tilting of ~9° with respect to **c***, which is consistent with the values found in this work.

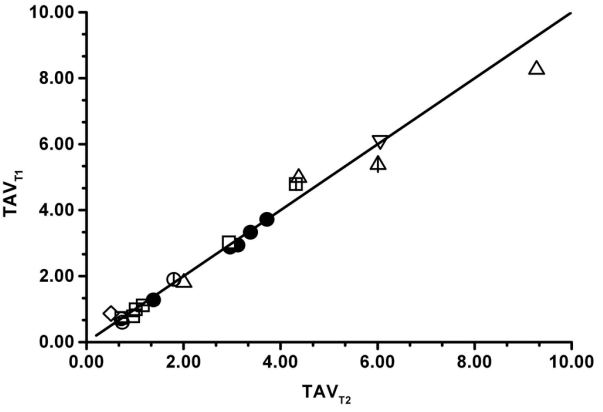

FIGURE 6. Comparison between the tetrahedral angle variance for the T1 and T2 sites (TAV_{T1} vs. TAV_{T2}). The 1:1 line is shown. Symbols as in Figure 1.

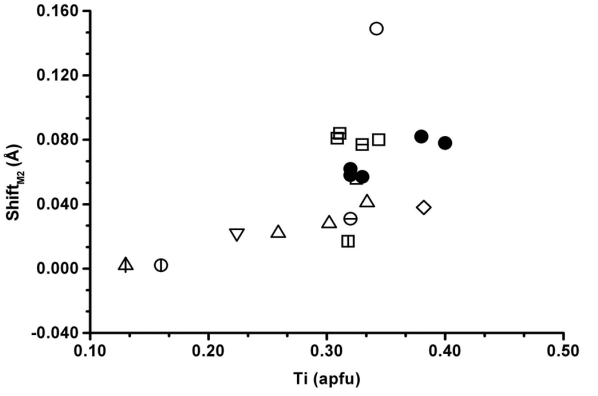

FIGURE 7. Plot of the shift of M2 cation ($shift_{M2}$) vs. Ti content. Symbols as in Figure 1. Data from Bohlen et al. (1980), Bigi et al. (1993), Bigi and Brigatti (1994), Brigatti et al. (2000, 2005, 2008), and Pini et al. (2008) are essentially affected by Ti-oxy substitution and exhibit a good correlation (R = 0.90) between the plotted parameters; the remaining data have different relative extent of Ti-oxy and Fe^{3+}-oxy substitutions.

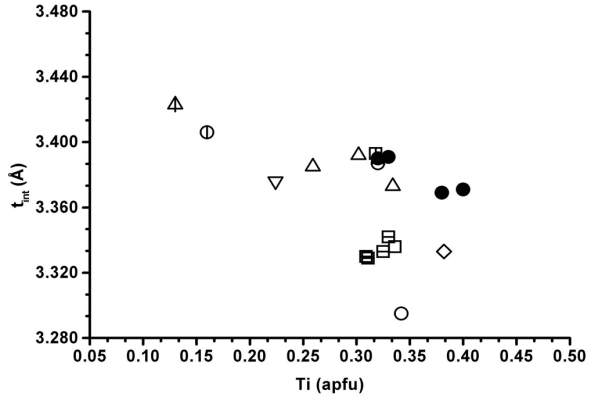

FIGURE 8. Plot of interlayer thickness (t_{int}) vs. Ti content. Symbols as in Figure 1.

These values for the hydroxyl orientation in 2M_1 micas are also similar to those reported for 1*M* micas from SCXRD (Ferraris et al. 2001; Schingaro et al. 2001; Scordari et al. 2006) and neutron diffraction studies (Ventruti et al. 2009).

In conclusion, the differences in chemical composition between Group 1 and Group 2 crystals studied here do not seem to have any influence on the growth mechanisms of the micas, which all resulted in 2M_1 polytypes. This result is in agreement with the literature, where close chemical similarities have been reported for coexisting 2M_1 and 1*M* micas (Takeda and Ross 1975; Bigi and Brigatti 1994; Laurora et al. 2007; Brigatti et al. 2008). It is noteworthy that Ti-phlogopites from ultrapotassic rocks of the volcanic fields (Bunyaruguru, Kasenyi, Katwe-Kikorongo) in the central portion of southwest Uganda exhibit different polytypes. For instance, in contrast to the BU3 kamafugite investigated here, other rock samples from Bunyaruguru have coexisting 1*M* and 2M_1 micas (with a predominance of 1*M*); rocks from Kasenyi show the coexistence of 1*M*, 2M_1, and 3*T* micas (with a prevalence of 2M_1); different mixtures of mica polytypes occur in kamafugites from Katwe–Kikorongo (Scordari et al. 2010b and unpublished results). Further investigations are under way to study in detail the crystal chemistry of micas from Ugandan kamafugites, as well as from other localities worldwide (Cupaello and Grotta del Cervo, Italy; Presidente Olegario, Brazil) with the kamafugite or the kamafugite–carbonatite association and different geodynamic settings (Bailey and Collier 2000; Eby et al. 2003; Tappe et al. 2003; Stoppa et al. 2003). A comparative crystal chemical analysis of phlogopites that occur in such rare lithologies may, indeed, complement petrological, geochemical, and geological data to gain deeper insight into debated issues such as the origin of potassic and ultrapotassic magmatism, the causes of heterogeneities in host magma composition and their relationships with the geodynamic setting (see for instances Lloyd et al. 2002; Eby et al. 2003; Avanzinelli et al. 2009 and references therein).

Acknowledgments

The authors thank Stefano Poli (University of Milano) for use of the facilities at the Electron Microprobe Laboratory at the Dipartimento di Scienze della Terra, Università di Milano, and Francesco Stoppa for providing the rock sample. Giuseppe Pedrazzi is gratefully acknowledged for performing Mössbauer analysis. The authors are also grateful to D. Gatta and an anonymous referee for their helpful comments. This work was funded by the COFIN-MIUR.

References cited

Aldega, L., Cuadros, J., Laurora, A., and Rossi, A. (2009) Weathering of phlogopite to beidellite in a karsitic environment. American Journal of Science, 309, 689–710.

Avanzinelli, R., Lustrino, M., Mattei, M., Melluso, L., and Conticelli, S. (2009) Potassic and ultrapotassic magmatism in the circum-Tyrrhenian region: Significance of carbonated pelitic vs. pelitic sediment recycling at destructive plate margins. Lithos, 113, 213–227.

Bailey, S.W. (1984a) Classification and structures of the micas. In S.W. Baley, Ed., Micas, 13, p. 1–12. Reviews in Mineralogy, Mineralogical Society of America, Chantilly, Virginia.

——— (1984b) Crystal chemistry of the true micas. In S.W. Baley, Ed., Micas, 13, p. 13–61. Reviews in Mineralogy, Mineralogical Society of America, Chantilly, Virginia.

——— (1984c) Review of cation ordering in micas. Clays and Clay Minerals, 32, 81–92.

Bailey, D.K. and Collier, J.D. (2000) Carbonatite-melilitite association in the Italian collision zone and the Ugandan rifted craton: significant common factors. Mineralogical Magazine, 64, 675–682.

Betteridge, P.W., Carruthers, J.R., Cooper, R.I., Prout, K., and Watkin, D.J. (2003) Crystals version 12: software for guided crystal structure analysis. Journal of Applied Crystallography, 36, 1487.

Bigi, S. and Brigatti, M.F. (1994) Crystal chemistry and microstructures of plutonic biotite. American Mineralogist, 79, 63–72.

Bigi, S., Brigatti, M.F., Mazzucchelli, M., and Rivalenti, G. (1993) Crystal chemical variations in Ba-rich biotites from gabbroic rocks of lower crust (Ivrea Zone, NW Italy). Contributions to Mineralogy and Petrology, 113, 87–99.

Bohlen, S.R., Peacor, D.R., and Essene, E.J. (1980) Crystal chemistry of a metamorphic biotite and its significance in water barometry. American Mineralogist, 65, 55–62.

Brigatti, M.F., Frigieri, P., Ghezzo, C., and Poppi, L. (2000) Crystal chemistry of Al-rich biotites coexisting with muscovites in peraluminous granites. American Mineralogist, 85, 436–448.

Brigatti, M.F., Caprilli, E., Funiciello, R., Giordano, G., Mottana, A., and Poppi, L. (2005) Crystal chemistry of ferroan phlogopites from the Albano maar lake (Colli Albani volcano, central Italy). European Journal of Mineralogy, 17, 611–621.

Brigatti, M.F., Guidotti, C.V., Malferrari, D., and Sassi, F.P. (2008) Single-crystal X-ray studies of trioctahedral micas coexisting with dioctahedral micas in metamorphic sequences from western Maine. American Mineralogist, 93, 396–408.

Bruker (2003a) SAINT. Bruker AXS Inc., Madison, Wisconsin.

——— (2003b) APEX2. Bruker AXS Inc., Madison, Wisconsin.

Bujnowski, T., Guggenheim, S., and Kato, T. (2009) Crystal structure determination of anandite-2*M* mica. American Mineralogist, 94, 1144–1152.

Cruciani, G. and Zanazzi, P.F. (1994) Cation partitioning and substitution mechanisms in 1*M* phlogopite: A crystal chemical study. American Mineralogist, 79, 289–301.

Donnay, G., Morimoto, N., Takeda, H., and Donnay, J.D.H. (1964a) Trioctahedral one-layer micas. I. Crystal structure of a synthetic iron mica. Acta Crystallographica, 17, 1369–1373.

Donnay, G., Donnay, J.D.H., and Takeda, H. (1964b) Trioctahedral one-layer micas. II. Prediction of the structure from composition and cell dimensions. Acta Crystallographica, 17, 1374–1381.

Ďurovíč, S. (1994) Classification of phyllosilicates according to the symmetry of their octahedral sheets. Ceramics—Silikáty, 38, 81–84.

Dyar, M.D. (2002) Optical and Mössbauer spectroscopy of iron in micas. In A. Mottana, F.P. Sassi, J.B. Thompson Jr., and S. Guggenheim, Eds., Micas: Crystal Chemistry and Metamorphic Petrology, 46, p. 313–349. Reviews in Mineralogy and Geochemistry, Mineralogical Society of America and the Geochemical Society, Chantilly, Virginia.

Eby, G.N., Lloyd, F.E., Woolley, A.R., Stoppa, F., and Weaver, S.D. (2003) Geochemistry and Mantle Source(s) for Carbonatitic and Potassic Lavas, Western Branch of the East-African Rift System, SW Uganda. GeoLines, 15, 23–27.

Ferraris, G., Gula, A., Ivaldi, G., Nespolo, M., Sokolova, E., Uvarova, Y., and Khomyakov, A.P. (2001) First structure determination of an MDO-2*O* mica polytype associated with a 1*M* polytype. European Journal of Mineralogy, 13, 1013–1023.

Giese, R.F. (1979) Hydroxyl orientations in 2:1 phyllosilicates. Clays and Clay Minerals, 27, 213–223.

Güven, N. (1971) The crystal structure of 2M_1 phengite and 2M_1 muscovite. Zeitschrift für Kristallographie, 134, 196–212.

Hazen, R.M. and Burnham, C.W. (1973) The crystal structures of one-layer phlogopite and annite. American Mineralogist, 58, 889–900.

Lacalamita, M. (2009) Studio chimico-strutturale dei siti anionico e cationici in miche triottaedriche a temperatura ambiente e non, 228 p. Ph.D. thesis, University of Bari, Italy.

Lacalamita, M., Schingaro, E., Scordari, F., Ventruti, G., Fabbrizio, A., and Pedrazzi, G. (2011) Substitution mechanisms and implications for the estimate of water fugacity for Ti-rich phlogopite from Mt. Vulture, Potenza, Italy. American Mineralogist, 96, 1381–1391, DOI: 10.2138/am.2011.3772.

Lagarec, K. and Rancourt, D.G. (1997) Extended Voigt-based analytic lineshape method for determining *N*-dimensional correlated hyperfine parameter distributions in Mössbauer spectroscopy. Nuclear Instruments and Methods in Physics Research B, 129, 266–280.

——— (1998) RECOIL, Mössbauer Spectral Analysis Software for Windows (version 1.0). Department of Physics, University of Ottawa, Canada.

Lahti, S.I. and Saikkonen, R. (1985) Bityite 2M_1 from Eräjärvi compared with related Li-Be brittle micas. Bulletin of the Geological Society of Finland, 57, 207–215.

Laurora, A., Brigatti, M.F., Mottana, A., Malferrari, D., and Caprilli, E. (2007) Crystal chemistry of trioctahedral micas in alkaline and subalkaline volcanic rocks: A case study from Mt. Sassetto (Tolfa district, Latium, central Italy). American Mineralogist, 92, 468–480.

Libowitzky, E. and Beran, A. (2004) IR spectroscopic characterization of hydrous species in minerals. In A. Beran and E. Libowitzky, Eds., Spectroscopic methods in Mineralogy, 6, p. 227–279. EMU Notes in Mineralogy, Eötvös University Press, Budapest.

Lloyd, F.E., Woolley, A.R., Stoppa, F., and Eby, G.N. (1999) Rift valley magma-

tism—is there evidence for laterally variable alkali clinopyroxenite mantle? GeoLines, 9, 76–83.
——— (2002) Phlogopite-biotite parageneses from the K-mafic-carbonatite effusive magmatic association of Katwe-Kikorongo, SW Uganda. Mineralogy and Petrology, 74, 299–322.
Mugnai, M. (2003) Il distretto vulcanico e geochimico delle province magmatiche di Toro Ankole e Bufumbira (Uganda), 246 p. Degree thesis, University of Chieti, Italy.
Murav'eva, N.S. and Senin, V.G. (2009) Carbonate–silicate equilibria in the high-magnesia ultrapotassic volcanics of the Toro-Ankole Province (Eastern African Rift Zone). Geochemistry International, 47, 882–900 (translated from Geokhimiya, 9, 937–957).
Nespolo, M. (1999) Analysis of family reflections of OD mica polytypes, and its application to twin identification. Mineralogical Journal, 21, 53–85.
Ohta, T., Takeda, H., and Takéuchi, Y. (1982) Mica polytypism: similarities in the crystal structures of coexisting 1M and 2M_1 oxybiotite. American Mineralogist, 67, 298–310.
Pini, S., Affronte, M., and Brigatti, M.F. (2008) Magnetic behaviour of trioctahedral mica-2M_1 occurring in a magnetic anomaly zone. Mineralogical Magazine, 72, 1035–1042.
Rancourt, D.G. and Ping, J.Y. (1991) Voigt-based methods for arbitrary-shape static hyperfine parameter distributions in Mössbauer spectroscopy. Nuclear Instruments and Methods in Physics Research, B, 58, 85–97.
Rancourt, D.G., Dang, M.-Z., and Lalonde, A.E. (1992) Mössbauer spectroscopy of tetrahedral Fe^{3+} in trioctahedral micas. American Mineralogist, 77, 34–43.
Rancourt, D.G., Christie, I.A.D., Royer, M., Kodama, H., Robert, J.-L., Lalonde, A.E., and Murad, E. (1994a) Determination of accurate $^{[4]}Fe^{3+}$, $^{[6]}Fe^{3+}$, and $^{[6]}Fe^{2+}$ site populations in synthetic annite by Mössbauer spectroscopy. American Mineralogist, 79, 51–62.
Rancourt, D.G., Ping, J.Y., and Berman, R.G. (1994b) Mössbauer spectroscopy of minerals. III. Octahedral-site Fe^{2+} quadrupole splitting distributions in the phlogopite-annite series. Physics and Chemistry of Minerals, 21, 258–267.
Rancourt, D.G., Ping, J.Y., Boukili, B., and Robert, J.-L. (1996) Octahedral-site Fe^{2+} quadrupole splitting distributions from Mössbauer spectroscopy along the (OH, F)-annite join. Physics and Chemistry of Minerals, 23, 63–71.
Redhammer, G.J. (1998) Characterisation of synthetic trioctahedral micas by Mössbauer spectroscopy. Hyperfine Interactions, 117, 85–115.
Redhammer, G.J., Beran, A., Schneider, J., Amthauer, G., and Lottermoser, W. (2000) Spectroscopic and structural properties of synthetic micas on the annite-siderophyllite binary: Synthesis, crystal structure refinement, Mössbauer, and infrared spectroscopy. American Mineralogist, 85, 449–465.
Redhammer, G.J., Amthauer, G., Lottermoser, W., Bernroider, M., Tippelt, G., and Roth, G. (2005) X-ray powder diffraction and ^{57}Fe-Mössbauer spectroscopy of synthetic trioctahedral micas $\{K\}[Me_3]<TSi_3>O_{10}(OH)_2$, Me = Ni^{2+}, Mg^{2+}, Co^{2+}, Fe^{2+}; T = Al^{3+}, Fe^{3+}. Mineralogy and Petrology, 85, 89–115.
Renner, B. and Lehmann, G. (1986) Correlation of angular and bond length distortions in TO_4 units in crystals. Zeitschrift für Kristallographie, 175, 43–59.
Rieder, M., Hybler, J., Smrčok, L'U., and Weiss, Z. (1996) Refinement of the crystal structure of zinnwaldite 2M_1. European Journal of Mineralogy, 8, 1241–1248.
Robinson, K., Gibbs, G.V., and Ribbe, P.H. (1971) Quadratic elongation: A quantitative measure of distortion in coordination polyhedra. Science, 172, 567–570.
Schingaro, E., Scordari, F., and Ventruti, G. (2001) Trioctahedral micas-1M from Mt. Vulture (Italy): Structural disorder and crystal chemistry. European Journal of Mineralogy, 13, 1057–1069.
Schingaro, E., Lacalamita, M., Scordari, F., Brigatti, M.F., and Pedrazzi, G. (2011) Crystal chemistry of Ti-rich fluorophlogopite from Presidente Olegario, Alto Paranaíba igneous province, Brazil. American Mineralogist, 96, 732–743.
Scordari, F., Ventruti, G., Sabato, A., Bellatreccia, F., Della Ventura, G., and Pedrazzi, G. (2006) Ti-rich phlogopite from Mt. Vulture (Potenza, Italy) investigated by a multianalytical approach: substitutional mechanisms and orientation of the OH dipoles. European Journal of Mineralogy, 18, 379–391.
Scordari, F., Dyar, M.D., Schingaro, E., Lacalamita, M., and Ottolini, L. (2010a) XRD, micro-XANES, EMPA, and SIMS investigation on phlogopite single crystals from Mt. Vulture (Italy). American Mineralogist, 95, 1657–1670.
Scordari, F., Schingaro, E., Mesto, E., and Lacalamita, M. (2010b) Coexistence of 1M and 2M_1 polytypes in Ti-phlogopite from the Central Fields volcanics of the Southwest Uganda. In E. Pál-Molnár, Ed., Acta Mineralogica-Petrographica Abstract Series, IMA2010 20th General Meeting of the International Mineralogical Association, 745. Department of Mineralogy, Geochemistry and Petrology, University of Szeged, Hungary.
Shannon, R.D. (1976) Revised effective ionic radii and systematic studies of interatomic distances in halides and chalcogenides. Acta Crystallogaphica, A32, 751–767.
Sheldrick, G.M. (2003) SADABS, Program for Empirical Absorption Correction of Area Detector Data. University of Göttingen, Germany.
Slade, P.G. and Radoslovich, E.W. (1985) The structure of an ephesite-2M_1 in space group *Cc.* Neues Jahrbuch für Mineralogie Monatshefte, 8, 337–352.
Slade, P.G., Schultz, P.K., and Dean, C. (1987) Refinement of the ephesite structure in *C*1 symmetry. Neues Jahrbuch für Mineralogie Monatshefte, 6, 275–287.
Smith, J.V. and Yoder, H.S. (1956) Experimental and theoretical studies of the mica polymorphs. Mineralogical Magazine, 31, 209–231.
Stoppa, F., Lloyd, F.E., and Rosatelli, G. (2003) CO_2 as the virtual propellant of carbonatite-kamafugite conjugate pairs and the eruption of diatremic tuffisite. Periodico di Mineralogia, 72, Special Issue Eurocarb, 1–18.
Takeda, H. and Ross, M. (1975) Mica polytypism: Dissimilarities in the crystal Structures of coexisting 1M and 2M_1 biotite. American Mineralogist, 60, 1030–1040.
Tappe, S., Foley, S.F., and Pearson, D.G. (2003) The Kamafugites of Uganda: a mineralogical and geochemical comparison with their Italian and Brazilian analogues. Periodico di Mineralogia, 72, Special Issue Eurocarb, 51–77.
Tischendorf, G., Rieder, M., Förster, H.-J., Gottesmann, B., and Guidotti, Ch.V. (2004) A new graphical presentation and subdivision of potassium micas. Mineralogical Magazine, 68, 649–667.
Toraya, H. (1981) Distortions of octahedra and octahedral sheets in 1M micas and the relation to their stability. Zeitschrift für Kristallographie, 157, 173–190.
Ventruti, G., Zema, M., Scordari, F., and Pedrazzi, G. (2008) Thermal behavior of a Ti-rich phlogopite from Mt. Vulture (Potenza, Italy): An in situ X-ray single-crystal diffraction study. American Mineralogist, 93, 632–643.
Ventruti, G., Levy, D., Pavese, A., Scordari, F., and Suard, E. (2009) High-temperature treatment, hydrogen behaviour and cation partitioning of a Fe-Ti bearing volcanic phlogopite by *in situ* neutron powder diffraction and FTIR spectroscopy. European Journal of Mineralogy, 21, 385–396.
Weiss, Z., Rieder, M., Chmielová, M., and Krajíček, J. (1985) Geometry of the octahedral coordination in micas: a review of refined structures. American Mineralogist, 70, 747–757.
Weiss, Z., Rieder, M., and Chmielová, M. (1992) Deformation of coordination polyhedra and their sheets in phyllosilicates. European Journal of Mineralogy, 4, 665–682.

Manuscript received May 27, 2011
Manuscript accepted October 13, 2011
Manuscript handled by M. Darby Dyar